Available online at www.sciencedirect.com
SCIENCE DIRECT®
PERGAMON
International Journal of Multiphase Flow 29 (2003) 1355–1372
International Journal of Multiphase Flow
www.elsevier.com/locate/ijmulflow

Brief communication

The motion of fibers in an evolving mixing layer

Jianzhong Lin [a,*], Xing Shi [a], Zhaosheng Yu [b]

[a] *Department of Mechanics, The State Key Laboratory of Fluid Power Transmission and Control, Zhejiang University, Hangzhou 310027, PR China*

[b] *Department of Mechanical and Mechatronic Engineering, University of Sydney, NSW 2006, Australia*

Received 23 July 2002; received in revised form 13 April 2003

1. Introduction

Particle-laden two-phase flows involving non-spherical particles such as aerosols and fibers are very common in many industrial processes. Over the past decade, the transport of non-spherical particles in flows has received much attention. In the following, we give a brief review on the works related to shear flows, sedimentation and turbulent flows.

1.1. Shear flow

Jeffery (1922) analyzed theoretically the motion of an ellipsoid in simple shear flow at zero Reynolds number, and he found that the ellipsoid rotated about the vorticity-axis (perpendicular to the flow-gradient plane) along a closed orbit, with the choice of orbit being dependent solely on the initial condition. Bretherton (1962) extended Jeffery's solution to all axisymmetric particles by simply replacing the aspect ratio of particles with an effective aspect ratio. When the effect of inertia was present, both the theory (Saffman, 1965) and the experiments (Karnis et al., 1966) revealed that the axis of a prolate spheroid gradually turned into flow-gradient plane, whereas a oblate spheroid eventually aligned its axis with the vorticity-axis. Recently, Ding and Aidun (2000) investigated numerically the effect of inertia on the dynamics of an elliptical cylinder and an ellipsoid suspended in shear flow with the Lattice–Boltzmann method. The rotational motion was confined to the flow-gradient plane and they found that the angular velocity of the particle decreased with increasing Reynolds number and the rotation stopped when the Reynolds number exceeded a critical value. Zettner and Yoda (2001) studied experimentally the effects of fluids inertia, geometry and flow confinement upon the dynamics of neutrally buoyant elliptical cylinders over a wide range of aspect ratios in simple shear flow at moderate shear Reynolds numbers, and the results confirmed that an

* Corresponding author.
E-mail address: mecjzlin@yahoo.com (J. Lin).

0301-9322/03/$ - see front matter
doi:10.1016/S0301-9322(03)00086-7

elliptical cylinder of moderate aspect ratio cease to rotate, resting at a nearly horizontal equilibrium orientation above a critical Reynolds number. It was observed that the axis of a fiber spiraled towards the vorticity axis in weakly elastic fluids, but the fixed orientation was along the flow direction in highly elastic fluids (e.g., Harlen nad Koch, 1993; Iso et al., 1996).

Both the translational and the rotational motions of a spheroid moving in shear flow near a wall were examined numerically by Gavze and Shapiro (1996, 1997, 1998) under the conditions that the fluids inertia was negligible, the effect of the particle inertia was present, and the rotation was confined to the flow-gradient plane. Broday et al. (1998) investigated the motion of both neutrally and non-neutrally buoyant prolate spheroidal particles in vertical shear flows at low Reynolds numbers by using the generalized Faxen law. Moses et al. (2001) inspected the motion of a fiber in a shear flow near a solid boundary experimentally. For the lateral migration of axisymmetric (but non-spherical) particles subjected to the effect of inertia, Leal (1980) concluded that they generally show the same behavior in all shear flows as a sphere provided that the data are averaged in time to remove any periodic lateral motion associated with the periodic rotation of the particle.

Rheology of fiber suspensions is a subject of extensive investigation, and a comprehensive review has been given by Petrie (1999). Recently, Petrich et al. (2000) examined experimentally the stress–microstructure relationship in semi-concentrated fiber suspensions. Raiskinmaki et al. (2000) studied the effects of the shape and concentration of the particles on the rheological properties of non-Brownian suspensions at non-zero Reynolds numbers with the Lattice–Boltzmann method.

1.2. Sedimentation

Unlike spheres, an isolated non-spherical particle falling in a fluid at zero Reynolds number can have motion perpendicular to gravity. The velocity of a slender body depends strongly on its orientation and can be evaluated with the slender body theory (Batchelor, 1970; Mackaplow and Shaqfeh, 1998). When the effect of inertia is present, a long body with the broadside across the stream is stable (e.g., Huang et al., 1994). Leal (1975) and Chiba et al. (1986) observed that a slender cylinder falling in a viscoelastic fluid rotated into a vertical orientation as a stable configuration. Liu and Joseph (1993) investigated extensively the effects of both inertia and viscoelasticity on the orientation of a long body. Huang et al. (1998) reported the numerical results on the sedimentation of an elliptic particle in Oldroyd-B fluids. The sedimentation of multi-cylinders at moderate Reynolds numbers were investigated experimentally by Jayaweera and Mason (1965) and Joseph (1993), and numerically by Qi (2001). The results showed that the wake of particles was important to the microstructure of suspensions. Turney et al. (1995), Herzhaft et al. (1996), Herzhaft and Guazzelli (1999), Mackaplow and Shaqfeh (1998), and Lin et al. (2002) studied the sedimentation of fiber (or cylinder) suspensions at low Reynolds numbers.

1.3. Turbulent flow

The works on the investigation of the interactions between spherical particles and turbulent flows showed that the distribution of particles is substantially affected by the coherent structures, and the turbulent structures are in turn modified by the presence of the particles (e.g., Yamamoto et al., 2001). Some works on the motion of non-spheroidic particles in wall-bounded shear flows

have been reported (Fan and Ahmadi, 1993; Soltani et al., 1997; Soltani and Ahmadi, 2000; Shams et al., 2001; Zhang et al., 2001), which revealed that the effect of the coherent structures on the particle dispersion was basically the same for all particles with different shapes. Johnson and Martonen (1993) studied the deposition of fibers in the pulmonary track of humans and animals. Fan and Ahmadi (1995), Olson and Kerekes (1988) and Olson (2001) considered the motion of ellipsoidal particles or fibers in homogeneous isotropic turbulent.

In turbulent shear flows, the effect of fluid inertia on the motion of particles generally exists, therefore, in the dilute case where the interaction between the particles can be neglected, the principal axis of an ellipsoid-like particle turns into the flow-gradient plane and the particle mainly rotates about the vorticity-axis. Since the particle of large aspect ratio spends most of its rotation time at the orientation of the flow direction, the particle appear to align its long axis with the flow direction. Zhang et al. (2001) numerically examined the motion of ellipsoids in a dilute turbulent channel flow, and it is interesting that he observed the same motion behavior of the ellipsoids as described above, although the inertia of the fluid was neglected for computation of the hydrodynamic drag on the particles. The reason is not clear, but it should be noted that the turbulent shear flow is not a steady simple shear flow, but an unsteady complex flow. The presence of extensional strain rate components in the velocity gradient could significantly affect the orientation of an ellipsoid, e.g., the steady orientation of a rod is along the flow direction in an extensional flow. In addition, the effect of the particle inertia could also qualitatively modify the motion behavior of the particle. For example, Gavze and Shapiro (1998) observed that an ellipsoid near a wall in a shear flow migrated towards the wall under the conditions that the fluids inertia was neglected and the effect of the particle inertia was considered. There should be no migration if the particle inertia is absent. The results presented in the current study also confirm that a fiber moving in an inhomogeneous flow turns into the flow-gradient plane and align with the flow direction, although the computation of the hydrodynamic force on the fiber is based on the Stokes flow theory.

The interactions between the particles would cause the dispersion of the orientation distribution, as described by the theory of fiber suspensions. Bernstein and Shapiro (1994) measured the orientation distribution function of glass fiber cylindrical particles suspended in laminar and turbulent shear flows, and the effect of the flow velocity gradients and the particle's rotational diffusivities on the orientation distribution function was examined.

As far as mixing layer flow is concerned, the experimental and computational works involving spherical particle transport were reported in the literature (e.g., Crowe et al., 1985; Hishida et al., 1992; Tong and Wang, 1999; Lin et al., 2000). However, the work on the transport of non-spherical particles has not been reported yet. Fiber is one of the most common non-spherical particles. In this paper, the spatial and orientation distributions of fibers moving in an evolving mixing layer are investigated. The reasons for taking a mixing layer as a background flow are listed as follows. (1) The mixing layer represents a typical shear flow and thus provides a building block for many practical inhomogeneous flows such as wakes and jets. (2) In the engineering applications, the particle dispersion in mixing layers is of importance, for example, a coal-fired power plant relies on the proper dispersion of particles in the feed jets to provide a well-mixed gas–particle flow for efficient combustion. The proper design of the flow processes depends heavily on the understanding of the dispersion of particles. (3) The mixing layer is a typical flow which involves the large-scale vortex structures. The traditional approach of dealing with the dispersion

of particles is to regard the process as a Fickian diffusion process and to quantify the mass transfer of particulates with a diffusion coefficient and a particle concentration gradient. This model may be adequate for near-isotropic turbulent flows, however, is not suited to the anisotropic turbulent flows such as a mixing layer.

The spatial and orientation distributions of fibers play an important role in determining the rheological properties, thermal conductivity, absorption and reflection of light, etc. (Brenner, 1974). The Stokes number, which is used to characterize the effectiveness of large-scale structures to move the particle laterally in a mixing layer, the fiber-to-fluid density ratio and the fiber aspect ratio are control parameters for the motion of fibers. The current study is aimed to provide the effects of these factors on the spatial and orientation distributions of fibers.

2. Physical model and governing equations

2.1. Mixing layer

Fig. 1 shows a schematic of the standard Newtonian fluid mixing layer consisting of two parallel streams with different velocities U_1 and U_2. We take $u_0 = (U_1 - U_2)/2$ as the free stream velocity in a reference frame that moves at the average velocity of the flow $(U_1 + U_2)/2$ and θ_0 as the momentum thickness of the mixing layer. We use $2u_0$ and θ_0 as characteristic velocity and characteristic length to make the equations dimensionless and define the Reynolds number by $Re = (U_1 - U_2)\theta_0/v$.

The governing equations in the physical space are the continuity equation and the momentum equation:

$$\nabla \cdot \mathbf{u} = 0 \tag{1}$$

$$\frac{\partial \mathbf{u}}{\partial t} + \boldsymbol{\omega} \times \mathbf{u} = -\nabla P + \frac{1}{Re}\nabla^2 \mathbf{u} \tag{2}$$

where $\boldsymbol{\omega} = \nabla \times \mathbf{u}$ is the vorticity, $P = p + \frac{1}{2}|\mathbf{u}|^2$ is the total pressure.

We are interested in the time-developing mixing layer since it can be thought of as an approximation to spatially developing mixing layer (Rogers and Moser, 1992) and the simulation of time-developing mixing layer allows much higher resolution of computation. For the time-developing mixing layer, we can impose periodic boundary conditions in the streamwise direction.

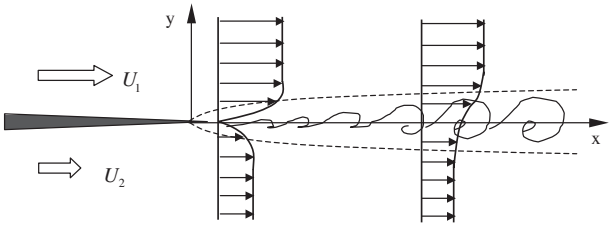

Fig. 1. Schematics of mixing layer.

Considering that all the perturbations vanish rapidly as $y \to \infty$, periodic conditions can be also imposed in the transverse direction by introducing the image flows far enough from the mixing layer center. Thus, the standard Fourier pseudo-spectral method can be applied directly.

The initial velocity is for the time-developing mixing layer consists of the following two parts:

(1) The base flow with hyperbolic-tangent profile

$$U = 0.5\tanh(y) \tag{3}$$

(2) The two-dimensional fundamental disturbances, the streamfunction of which is

$$\psi_z(x,y) = A_1 \Re[\phi_1(y) e^{i\alpha_1 x}] \tag{4}$$

where $\Re$ denotes an operator that gets the real part for a complex. A_1 is the amplitude of the disturbance, α_1 represents the wavenumber for fundamental disturbances and $\phi_1(y)$ denotes the normalized eigenfunction for the fundamentals, which can be approximately derived from the inviscid linear stability theory in the case of high Reynolds numbers. The value for α_1 in this study is set to be 0.4446 which corresponds to the most unstable perturbation given by Michalke (1964). We fix $A_1 = 0.1$ in this paper.

For convenience, we define $\mathbf{F} = \boldsymbol{\omega} \times \mathbf{u}$ and transform $\mathbf{u}, P, \mathbf{F}$ into the Fourier spectral space and denote them by $\mathbf{u}^*$, p^* and $\mathbf{F}^*$, respectively. Then Eqs. (1) and (2) in the spectral space with p^* eliminated read

$$\boldsymbol{\alpha} \cdot \mathbf{u}^* = 0 \tag{5}$$

$$\left(\frac{\mathrm{d}}{\mathrm{d}t} + \frac{\boldsymbol{\alpha}\cdot\boldsymbol{\alpha}}{Re}\right)\mathbf{u}^* = \frac{\boldsymbol{\alpha}(\boldsymbol{\alpha}\cdot\mathbf{F}^*)}{\boldsymbol{\alpha}\cdot\boldsymbol{\alpha}} - \mathbf{F}^* \tag{6}$$

where $\boldsymbol{\alpha} = (\alpha_1, \alpha_2, \alpha_3) = (2\pi k_1/L_1, 2\pi k_2/L_2, 2\pi k_3/L_3)$, L_1, L_2, L_3 are the periods in the streamwise, transverse and spanwise directions, respectively. k_1, k_2, k_3 are the wave numbers in three directions, respectively. Eq. (6) is solved by using the Adams-Bashforth scheme for the terms of the right-hand side and the implicit Crank–Nicolson scheme for the terms of the left-hand side. Time step Δt is 0.05. The numbers of the streamwise, transverse and spanwise collocation points are taken to be 64, 128 and 32, respectively.

2.2. Motion of fibers

The fibers have a length $2l$, a radius a, and density ρ_p. The calculation of the motion of fibers is based on the following assumptions:

(1) The fibers are non-Brownian rigid particles.
(2) The flow around each fiber is considered as the Stokes flow.
(3) The size of each fiber is much smaller than the scale of the flow field.
(4) The interactions between fibers are neglected.

Based on the assumptions above, the slender body theory (Batchelor, 1970) can be used to represent the disturbance velocity created by a fiber as an integral of Stokeslets distributed along

the fiber axis. Then the motion of the fibers in a particulate flow satisfies the following equation (Mackaplow and Shaqfeh, 1998):

$$\mathbf{U}+(\boldsymbol{\Omega}\times s\mathbf{p})-\mathbf{u}^{\infty}(\mathbf{x}_{\mathbf{c}}+s\mathbf{p})=-2\left(\ln 2A+\ln\frac{\sqrt{1-s^2}}{b(s)}\right)(\boldsymbol{\delta}+\mathbf{pp})\cdot\mathbf{f}(s) - (\boldsymbol{\delta}-3\mathbf{pp})\cdot\mathbf{f}(s)-(\boldsymbol{\delta}+\mathbf{pp})\cdot\int\frac{\mathbf{f}(s)-\mathbf{f}(s')}{|s-s'|}\,\mathrm{d}s' \tag{7}$$

where $\mathbf{U}$ and Ω are the translational and angular velocity of fiber, $\mathbf{p}$ is the orientation unit vector of a fiber, s is the distance from the center of fiber, $\mathbf{u}^{\infty}$ is the undisturbed fluid velocity, $\mathbf{x}_{\mathrm{c}}$ is the fiber center position, A is fiber aspect ratio, b, a shape factor, equals unity for fiber, and $\mathbf{f}(s)$ is the density distribution of the force along the axis of a fiber. The integral in Eq. (7) is evaluated by 11-point Gauss-Legendre integration, and then $\mathbf{f}(s)$ is obtained by solving the resulting linear equations. The force and torque on a fiber are

$$\mathbf{F}=8\pi\mu l\int_{-1}^{1}\mathbf{f}(s)\,\mathrm{d}s,\quad \mathbf{T}=8\pi\mu l^2\int_{-1}^{1}s\mathbf{p}\times\mathbf{f}\,\mathrm{d}s \tag{8}$$

where μ is the fluid viscosity. The fiber's motion can be obtained by solving the following equations

$$m_p\frac{\mathrm{d}\mathbf{u}_p}{\mathrm{d}t}=\mathbf{F} \tag{9a}$$

$$\mathbf{I}\cdot\frac{\mathrm{d}\boldsymbol{\Omega}}{\mathrm{d}t}+\boldsymbol{\Omega}\times\mathbf{I}\cdot\boldsymbol{\Omega}=\mathbf{T} \tag{9b}$$

where m_p, $\mathbf{u}_p$ and $\mathbf{I}$ are fiber mass, velocity and moment of inertia, respectively. After non-dimensionlization with the scales of flow field, Eq. (9a) takes the form as

$$\frac{\mathrm{d}\mathbf{u}_p}{\mathrm{d}t}=\frac{1}{St}\int_{-1}^{1}\mathbf{f}(s)\,\mathrm{d}s \tag{10}$$

where the Stokes number is defined as $St=\rho_p a^2\Delta U/4\mu\theta_0$, θ_0 is the momentum thickness of the mixing layer. With the slender body assumption (the fiber aspect ratio $A\gg 1$), the three component equations of Eq. (9b) in the body coordinate system yield:

$$\frac{\mathrm{d}\Omega_x}{\mathrm{d}t}=\frac{3}{StA}\left(\frac{4St}{Re\rho^*}\right)^{-\frac{1}{2}}T_x+\Omega_y\Omega_z \tag{11a}$$

$$\frac{\mathrm{d}\Omega_y}{\mathrm{d}t}=\frac{3}{StA}\left(\frac{4St}{Re\rho^*}\right)^{-\frac{1}{2}}T_y-\Omega_z\Omega_x \tag{11b}$$

$$\frac{\mathrm{d}\Omega_z}{\mathrm{d}t}=\frac{2A}{St}\left(\frac{4St}{Re\rho^*}\right)^{-\frac{1}{2}}T_z \tag{11c}$$

where ρ^* is the fiber-to-fluid density ratio. From Eqs. (10) and (11) we find that the translational motion of a fiber is only determined by the Stokes number, whereas, the rotation of fiber is controlled by the fiber aspect ratio, the fiber-to-fluid density ratio and the Stokes number. The

effect of the density ratio at fixed Reynolds number and Stokes number can reflect the effect of the dimensionless size of the fiber, since

$$\frac{4St}{Re\rho^*} = \left(\frac{a}{\theta_0}\right)^2$$

3. Results and discussions

In the simulations, only a two-dimensional perturbation is introduced to the flow. It is obvious that the flow will keep homogeneous along the Z-axis, which is illustrated in Fig. 2. However, the motion of fibers is considered three-dimensional. The Reynolds number is fixed to be 400. The effect of gravity on the motion of fiber is neglected.

3.1. Vortex roll-up

The different stages of vorticity evolution are illustrated in Fig. 3. The Kelvin–Helmholtz instability leads to the roll-up of the mixing layer and the formation of a large-scale vortex. Using topological theory, the vortex center is a center-point and the center between two consecutive center-points is a saddle-point where vorticity is depleted. Because the inhomogeneity of the flow is important to the orientation of the fibers, it is necessary to divide the flow fields into two parts: inhomogeneous flow region and homogeneous flow region. For convenience, we choose the streamlines through the two neighboring saddle-points as the demarcation lines and regard the region encompassed by the streamlines (referred to as cat-eye zone from its shape) as the inhomogeneous flow region and the region outside the cat-eye zone as homogeneous flow region. It is worth noting that this demarcation of the inhomogeneous and homogeneous flow regions by the streamlines is not established precisely. The extensional strain region along the edge of the vortex is not entirely confined within the cat-eye zone. Moreover, the vorticity diffusion can enhance the area of inhomogeneous flow (see last two sub-plots in Fig. 3). Therefore, the actual inhomogeneous flow region is a bit larger than the cat-eye zone.

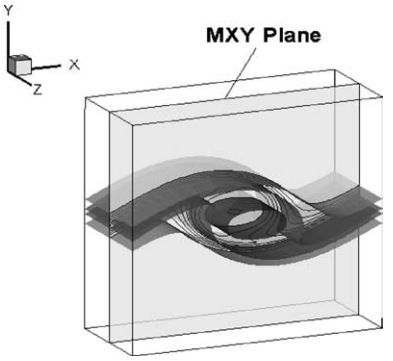

Fig. 2. Coordinate system of vortex roll-up.

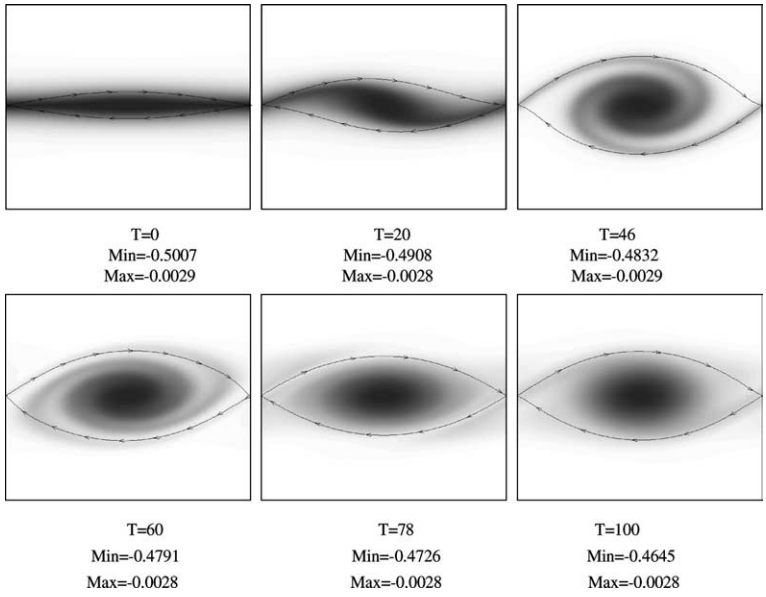

Fig. 3. Vorticity distributions (contours) at different times.

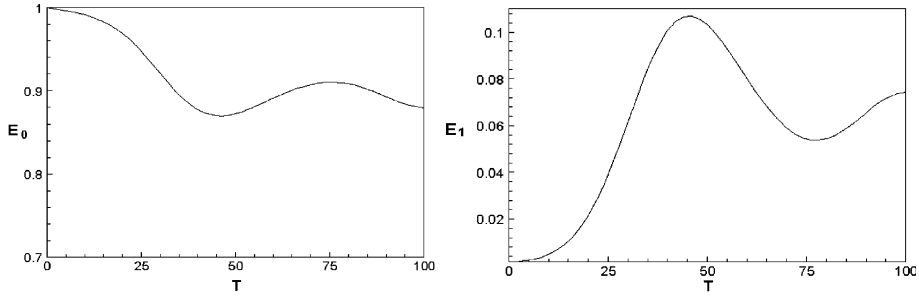

(a) Energy in the base flow (b) Energy in the fundamental perturbation

Fig. 4. Evolution of energy: (a) energy in the base flow, (b) energy in the fundamental perturbation.

Fig. 4 gives the evolution of the energy in the base flow and the fundamental perturbation. Firstly the fundamental perturbation gets energy from the base flow and amplifies exponentially. At $T = 46$, the energy of the fundamental perturbation reaches its maximum, which is customarily defined as the time of roll-up. During $T = 46$–78, part of the energy in the fundamental returns to the base flow. The flow then attains a quasi-steady state, which is characterized by the energy exchange between the base flow and the fundamental perturbation.

3.2. Comparison between the computations and the experiments

In order to verify the computation, we perform the corresponding experiments to compare with the numerical results. The experimental facility is shown in Fig. 5. The main parts of the facility

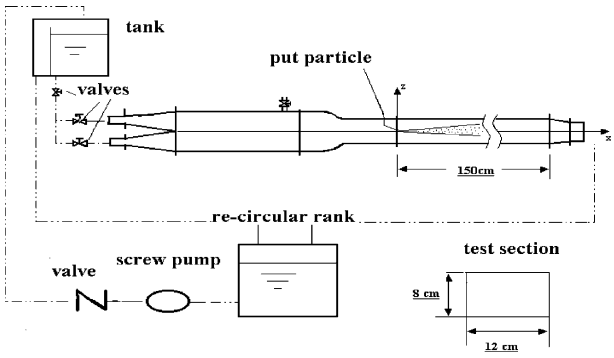

Fig. 5. Experimental facility.

are a reservoir, valves and test section. The size of the test section is 150 cm (length) × 12 cm (width) × 8 cm (height). The fluid passes through a straight duct that is 50 cm long and contains several screens, and through a 9:1 contraction duct with the length of 36 cm before reaching the test section. In the experiment, the velocities of the main streams are controlled by the adjustors at the input and the diffluent valves in the transmission sect. The nylon fibers with the diameter of 20 μm, the density of 1.04×10^3 kg/m^3 and the aspect ratio ranging from 20 to 50 are used. The fibers are injected into the upper flow. The velocity profile near the end of the splitter plate is measured by LDA and is shown in Fig. 6. The velocities of the upper and the lower main streams are 1.1 and 5.3 cm/s, respectively. Based on the velocity profile, the momentum thickness θ_0 is calculated as 0.42 cm. The Reynolds number is 175 and the Stokes number of fiber is 1.09×10^{-3}. The reason that experiment was performed at only one Stokes number is that the experiment just aims to verify the computational results, and the detailed results about the effect of Stokes number will be given by computation in 3.3. It is much more difficult to measure the orientation of the fibers in experiments.

The computational and experimental results for the spatial and orientation distributions of fibers at the comparable values of parameters are presented in Fig. 7. We can see that the computational results agree well with the experiments, and the motion behavior of the fibers in the mixing layer is essentially captured by the numerical simulation.

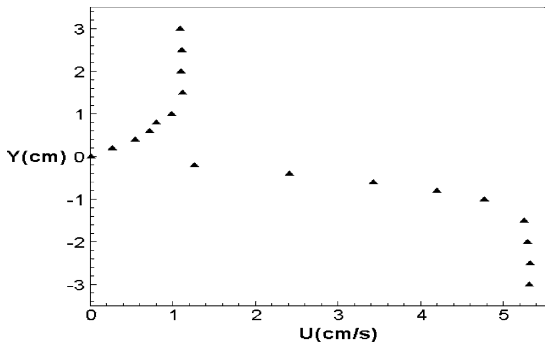

Fig. 6. The velocity profile at the inlet.

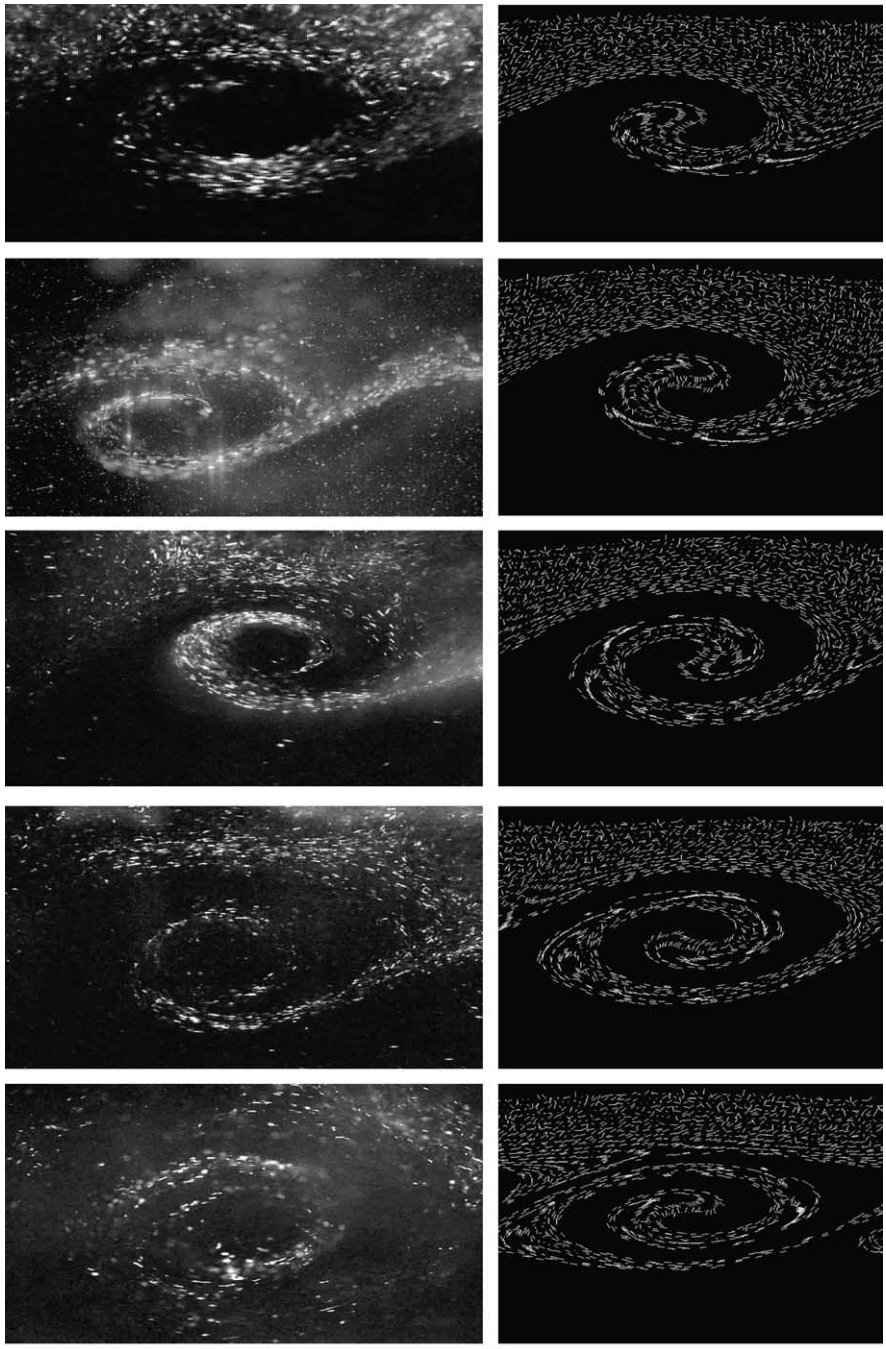

Fig. 7. Comparison between the computation and the experiment.

3.3. Effect of the Stokes number on the spatial and orientation distributions of fibers

For all cases in this section, the fibers have the aspect ratio 30 and the density ratio 755. The fibers are initially distributed homogenously in the space and take isotropic orientations.

Fig. 8 shows the projection of the fibers into the *MXY*-plane. The Stokes number (*St*) represents the ratio of the fiber response time to the characteristic time scale of flow, and in a sense, the particle inertia. When *St* is small, e.g., 0.01, the fibers respond rapidly to the flow and almost follow the motion of local fluid elements. During the vortex roll-up, the spatial distribution of fibers keeps homogenous. When *St* is moderate or large, the response of fibers to the flow becomes slow. The fibers in the vortex core region appear centrifugalized and are consequently concentrated at the edge of the vortex. At $St = 1.0$, almost all the fibers in the cat-eye zone are located at

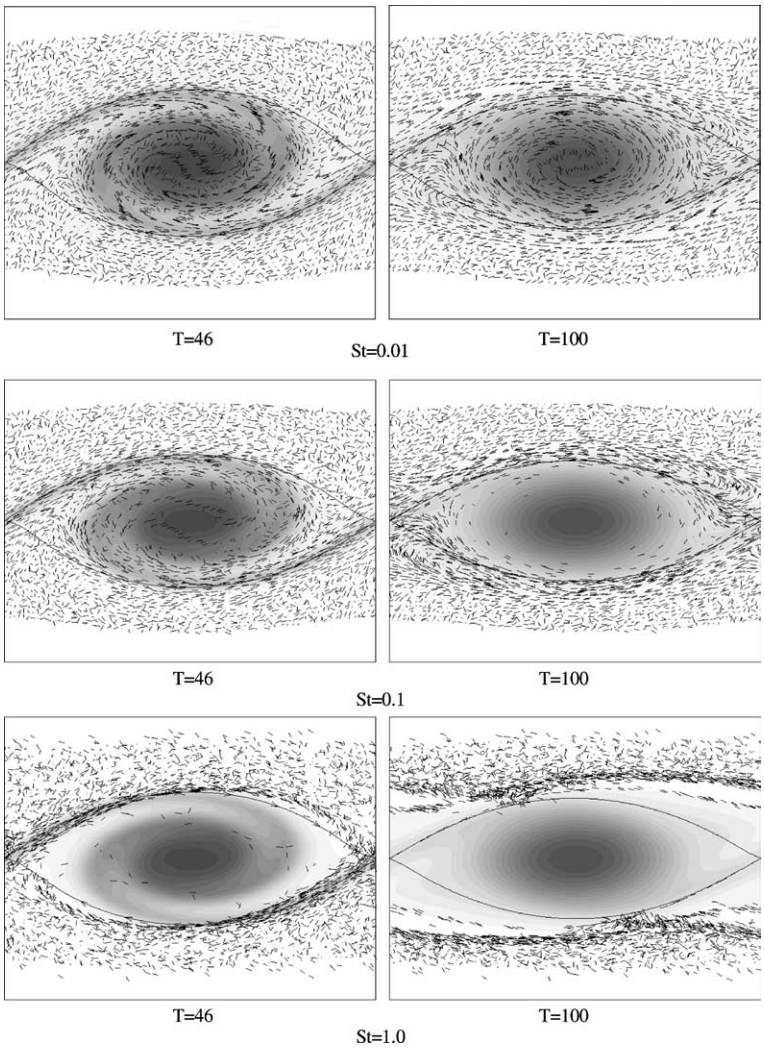

Fig. 8. Distributions of fibers at the different Stokes numbers.

the edge of the vortex. These results are similar to those given by Crowe et al. (1985) for the case of the spherical particles.

In order to do some quantitative analyses, we define the fibers centrifugation degree in the *MXY*-plane:

$$D_c(t) = \frac{1}{D_0} \sum_{i=1}^{N} \sqrt{(x_f(t) - x_c)^2 + (y_f(t) - y_c)^2} \tag{12}$$

where (x_f, y_f) is the projection of the center of a fiber into the *MXY*-plane, (x_c, y_c) is the coordinate of the vortex center and $D_0 = \sum_{i=1}^{N} \sqrt{(x_f(0) - x_c)^2 + (y_f(0) - y_c)^2}$.

It can be found in Fig. 9 that the larger the Stokes number is, the higher the centrifugation degree is, which is consistent with the qualitative analysis above.

Next, we investigate the behavior of fiber orientations. The distributions of angles between the axes of fibers and the *Z*-axis in the cat-eye zone and outside the cat-eye zone at $T = 100$ are shown in Figs. 10 and 11, respectively. We can see that there is no preferable orientation for the fibers outside the cat-eye zone and the fiber orientation keeps random, whereas in the cat-eye zone most fibers take the angle of $\pi/2$ with respect to the *Z*-axis, meaning that the fibers turn into the *XY*-plane. As mentioned in the Introduction section, it is interesting that the hydrodynamic force evaluated using the Stokes flow theory can give rise to the fibers rotating in the way as if subjected to the effect of inertia. The facts that the flow is not a steady simple shear flow here and the particle inertia is present may be responsible for this seemingly anomalous turn of the fibers. In addition, Figs. 10 and 11 show that the Stokes number has no significant effect on the orientation

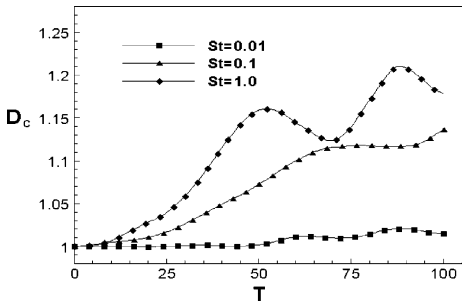

Fig. 9. Degree of centrifugation.

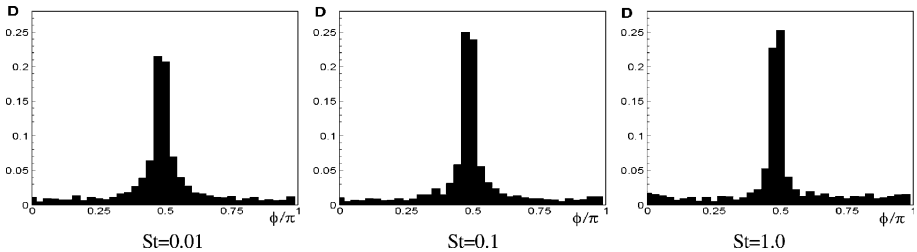

Fig. 10. Distributions of the angles between the fiber axes and the *Z*-axis in the cat-eye zone at $T = 100$.

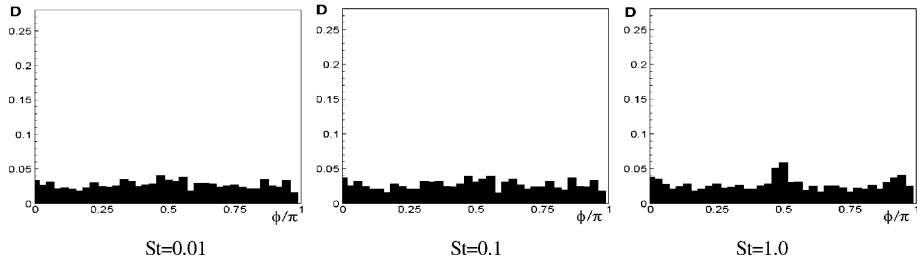

Fig. 11. Distributions of the angles between the fiber axes and the Z-axis in the outside cat-eye zone at $T = 100$.

distribution of fibers, although the distribution near the angle of $\pi/2$ is slightly more concentrated at larger Stokes numbers. From Fig. 8, most fibers in the inhomogeneous flow region appear to align with the flow direction. Since the flow dynamics is dominated by the vortex, we can say that the orientation of fibers in the XY-plane is dominated by the vortex. The Stokes number is defined globally as $St = \rho_p a^2 \Delta U / 4\mu\theta_0$ here, ΔU is the velocity difference of two streams and θ_0 the momentum thickness of the mixing layer, so the Stoles number does not affect the orientation. If the Stokes number is defined locally in terms of the shear rate, the conclusion may be different.

Apart from the motion in the XY-plane, the spanwise (along the Z-axis) drift of fibers is observed. The maximum drift $D_{z\max}$ and the average drift $\bar{D}_z$ are defined as

$$D_{z\max}(t) = \frac{1}{L} \max |Z_i(t) - Z_i(0)|, \quad i = 1, \ldots, N \tag{13}$$

$$\bar{D}_z(t) = \sqrt{\frac{1}{NL} \sum_{i=1}^{N} (Z_i(t) - Z_i(0))^2} \tag{14}$$

where $Z_i(t)$ is the Z-component of the position of the ith fiber, N is the total number of fibers, and L the streamwise length (period) of the flow. The reason why a fiber drifts in the spanwise direction is that a Z-component force on the fiber is generated when the axis of the fiber is not vertical or parallel to the Z-axis and the local flow is not homogeneous.

From Fig. 12, the drifts in all cases basically take place at the initial stage, and then the drift velocities become small, which is clearly caused by the turn of the fibers into the XY-plane and, for the case of large Stokes numbers, is partly due to the migration of fibers away from the

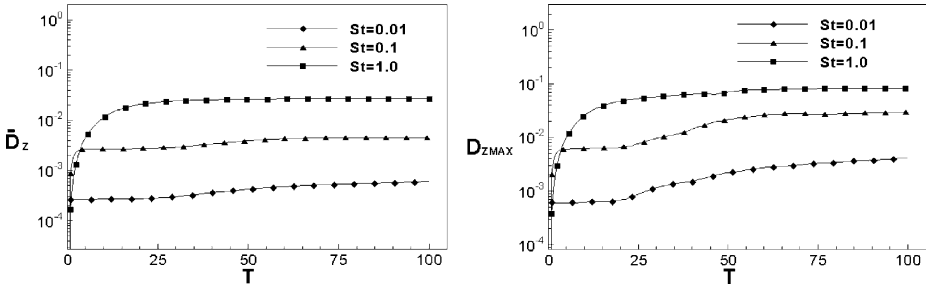

Fig. 12. Spanwise drifts of fibers.

cat-eye zone. Fig. 12 shows that the duration of the initial drift is longer, and consequently the total drift is more pronounced at a larger Stokes number. The longer initial drift at a higher Stokes number is probably due to the higher particle inertia, in the sense that it takes a longer time for a fiber of stronger inertia to cease its drift motion under the Stokes drag, although the generation of the drift motion at very initial time is slightly retarded at larger Stokes numbers, as shown in Fig. 12.

3.4. Effects of the density ratio on the spatial and orientation distributions of fibers

We investigate the effects of the density ratio on the spatial and orientation distributions of fibers at $St = 0.1$. The difference between the spatial and orientation distributions of fibers at two different density ratios, case 1 and 2, can be measured by the average position difference, $\bar{D}_l$, and the average angle difference, $\bar{D}_\theta$, which are defined, respectively, as

$$\bar{D}_l = \frac{1}{NL}\sum_{i=1}^{N} |\mathbf{x}_i^1 - \mathbf{x}_i^2| \tag{15}$$

$$\bar{D}_\theta = \frac{1}{N}\sum_{i=1}^{N} \arccos(|\mathbf{p}_1 \cdot \mathbf{p}_2|) \tag{16}$$

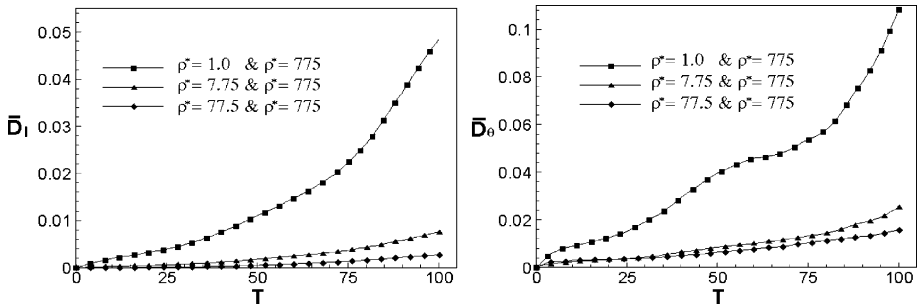

Fig. 13. Evolution of $\bar{D}_l$ and $\bar{D}_\theta$ of fibers at different density ratios.

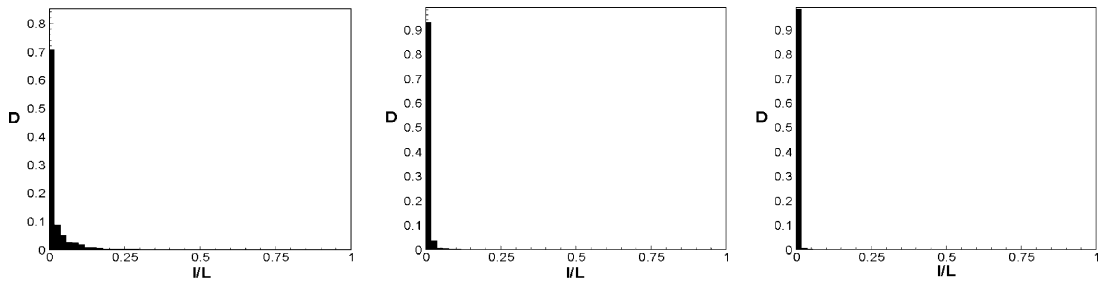

Fig. 14. Distributions of position differences ($T = 100$) at different density ratios.

where N is the total number of fibers, $\mathbf{x}_i^1$, $\mathbf{x}_i^2$ are the positions of the fibers with the same initial positions for the two cases studied, respectively, and L is the streamwise length.

The evolutions of $\bar{D}_l$ and $\bar{D}_\theta$ are shown in Fig. 13. Both of them increase monotonously with time and the density ratio difference between the two cases compared. From Figs. 14 and 15, which show the distributions of the position differences and the orientation differences, respectively, at $T = 100$, we find that the motion of most fibers is slightly affected by the density ratio and only some individual fibers have large position and orientation differences at the two different density ratios. In a word, the effect of density ratio is small.

3.5. Effects of the fiber aspect ratio on the spatial and orientation distributions of fibers

We also examine the functions of the fiber aspect ratio using the above method. The results are depicted in Figs. 16–18. The similar tendency is found: the differences increase with time and the aspect ratio difference between the two cases. The effect of the aspect ratio on the motion of fibers is also small, although it seems that the fiber aspect ratio has a little stronger effect than the density ratio.

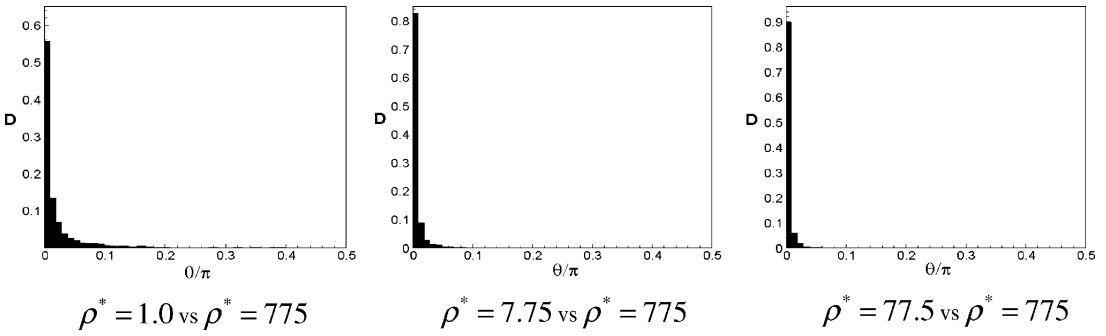

Fig. 15. Distributions of angle differences ($T = 100$) at different density ratios.

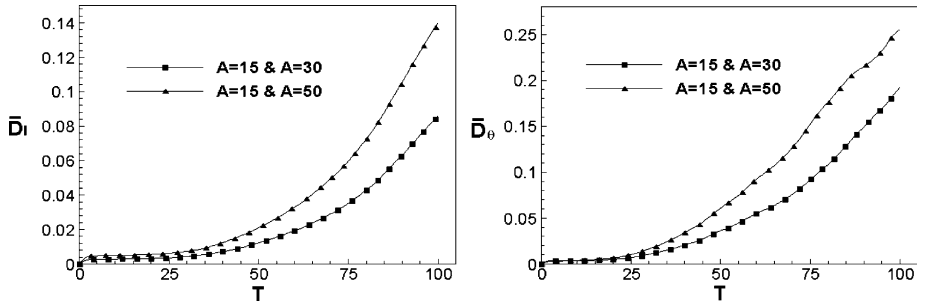

Fig. 16. Evolution of $\bar{D}_l$ and $\bar{D}_\theta$ of fibers at different aspect ratios.

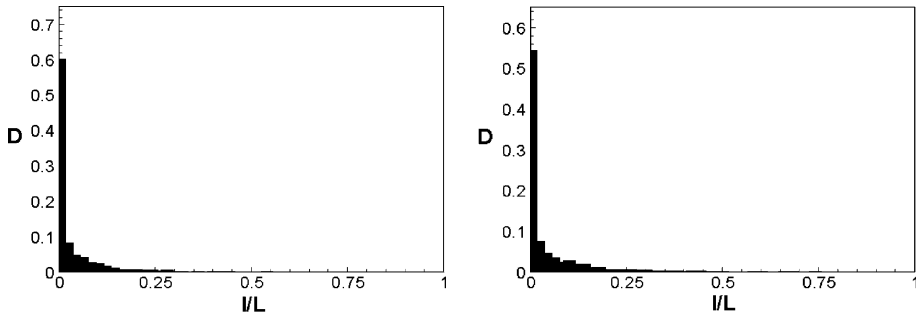

Fig. 17. Distributions of position differences ($T = 100$) at different aspect ratios.

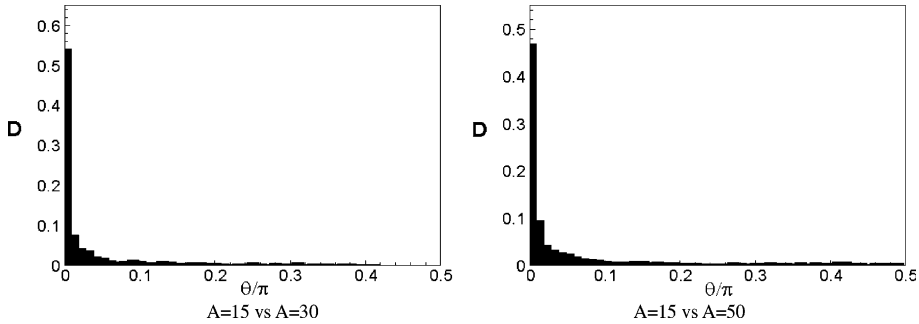

Fig. 18. Distributions of angle differences ($T = 100$) at different aspect ratios.

4. Conclusions

The effects of the Stokes number, the density ratio and the fiber aspect ratio on the spatial and orientation distributions of fibers in an evolving mixing layer are studied numerically, and the experiment confirms that the numerical results are reasonably correct. The following conclusions are drawn based on the discussions above:

(1) The Stokes number is the key parameter to determine the spatial distribution of fibers. At a small Stokes number the fibers are homogeneously distributed in the flow. When the Stokes number increases to O(0.1), the fibers migrate away from the large-scale vortex core region and are concentrated at the edge of the vortex.
(2) The spanwise drifts of the fibers basically take place at the initial stage. The amount of the spanwise drifts is increased as the Stokes number increases.
(3) The effect of the Stokes number on the orientation distribution of fibers is insignificant. Most fibers turn into the flow-gradient plane irrespective of the value of the Stokes number, and in the flow-gradient plane the fibers tend to align with the local flow direction, which is dominated by the large-scale vortex.
(4) The effects of both the density ratio and the fiber aspect ratio on the spatial and orientation distributions are small, although it seems that the latter is a little stronger than the former.

Acknowledgements

This research was supported by the National Natural Science Foundation of China (no. 19925210).

References

Batchelor, G.K., 1970. Slender-body theory for particles of arbitrary cross-section in Stokes flow. J. Fluid Mech., 44,419–44,440.

Bernstein, O., Shapiro, M., 1994. Direct determination of the orientation distribution function of cylindrical particles immersed in laminar and turbulent shear flows. J. Aerosol Sci. 25, 113–136.

Brenner, H., 1974. Rheology of a dilute suspension of axisymmetric Brownian particles. Int. J. Multiphase Flow 1, 195–218.

Bretherton, F.P., 1962. The motion of rigid particles in a shear flow at low Reynolds number. J. Fluid Mech. 14, 284–304.

Broday, D., Fichman, M., Shapiro, M., Gutfinger, C., 1998. Motion of spheroidal particles in vertical shear flows. Phys. Fluids 10, 86–100.

Chiba, K., Song, K., Horikawa, A., 1986. Motion of a slender body in quiescent polymer solutions. Rheol. Acta 25, 380–388.

Crowe, C.T., Gore, R.A., Troutt, T.R., 1985. Particle dispersion by coherent structures in free shear flows. Part. Sci. Tech. 3, 149–158.

Ding, E.-J., Aidun, C.K., 2000. The dynamics and scaling law for particles suspended in shear flow with inertia. J. Fluid Mech. 423, 317–344.

Fan, F.-G., Ahmadi, G., 1993. A sublayer model for turbulent deposition of particles in vertical ducts with smooth and rough surfaces. J. Aerosol Sci. 24, 45–64.

Fan, F.-G., Ahmadi, G., 1995. Dispersion of ellipsoidal particle in an isotropic pseudo-turbulent flow field. ASME J. Fluids Eng. 117, 154–161.

Gavze, E., Shapiro, M., 1996. Sedimentation of spheroidal particles in a vertical shear flow near a wall. J. Aerosol Sci. 27, S585–S596.

Gavze, E., Shapiro, M., 1997. Particles in a shear flow near a solid wall: effect of non-sphericity on forces and velocities. Int. J. Multiphase Flow 23, 155–182.

Gavze, E., Shapiro, M., 1998. Motion of inertial spheroidal particles in a shear flow near a solid wall with special application to aerosol transport in microgravity. J. Fluid Mech. 37, 59–79.

Harlen, O.G., Koch, L.L., 1993. Simple shear-flow of a suspension of fibers in a dilute polymer-soluton at high Deborah number. J. Fluid Mech. 252, 187–207.

Herzhaft, B., Guazzelli, E., 1999. Experimental study of the sedimentation of dilute and semi-dilute suspensions of fibres. J. Fluid Mech. 384, 133–158.

Herzhaft, B., Guazzelli, E., Michael, B.M., Shaqfeh, E.S.G., 1996. Experimental investigation of the sedimentation of a dilute fiber suspension. Phys. Rev. Lett. 77, 290–293.

Hishida, K., Ando, A., Maeda, M., 1992. Experiments on particle dispersion in a turbulent mixing layer. Int. J. Multiphase Flow 18, 181–194.

Huang, P.Y., Feng, J., Joseph, D.D., 1994. The turning couples on an elliptic particle settling in a vertical channel. J. Fluid Mech. 271, 1–28.

Huang, P.Y., Hu, H.H., Joseph, D.D., 1998. Direct simulation of the sedimentation of elliptic particles in Oldroyd-B fluids. J. Fluid Mech. 362, 297–325.

Iso, Y., Cohen, C., Koch, D.L., 1996. Orientation in simple shear flow of semi-dilute fiber suspensions 2. Highly elastic fluids. J. Non-Newton. Fluid Mech., 62,135–153.

Jayaweera, K.O.L.F., Mason, B.J., 1965. The behavior of freely falling cylinders and cones in a viscous fluid. J. Fluid Mech. 22, 709–720.

Jeffery, G.B., 1922. The motion of ellipsoidal particles immersed in a viscous fluid. Proc. Royal Soc. London A 102, 161–179.

Johnson, D.L., Martonen, T.B., 1993. Fiber deposition along airway walls: effects of fiber cross-section on rotational interception. J. Aerosol Sci. 24, 525–536.

Joseph, D.D., 1993. Finite size effects in fluidized suspension experiments. In: Roco, M.C. (Ed.), Particulate Two-Phase Flow. Butterworth–Heinemann, pp. 300–324.

Karnis, A., Goldsmith, H.L., Mason, S.G., 1966. The flow of suspensions through tubes V. Inertial effects. Can. J. Chem. Eng. 44, 181–193.

Leal, L.G., 1975. The slow motion of a slender rod-like particles in a second-order fluid. J. Fluid Mech., 69,305–69,337.

Leal, L.G., 1980. Particle motions in a viscous fluid. Ann. Rev. Fluid Mech., 12,435–12,476.

Lin, J.-Z., Shi, X., Yu, Z.-S., 2000. Research on the effect of particle of two-dimensional shear flow. Appl. Math. Mech. 21 (8), 855–860.

Lin, J.-Z., Wang, Y.-L., Wang, W.-X., Yu, Z.-S., 2002. Numerical simulation of the sedimentation of cylindrical pollutant particles in fluid. J. Environ. Sci. 14 (4), 433–438.

Liu, Y.J., Joseph, D.D., 1993. Sedimentation of particles in polymer solutions. J. Fluid Mech. 255, 565–595.

Mackaplow, M.B., Shaqfeh, E.S.G., 1998. A numerical study of the sedimentation of fiber suspension. J. Fluid Mech., 376,149–376,182.

Michalke, A., 1964. On the inviscid instability of the hyperbolic-tangent velocity profile. J. Fluid Mech. 19, 543–556.

Moses, K.B., Advani, S.G., Reinhardt, A., 2001. Investigation of fiber motion near solid boundaries in simple shear flow. Rheol. Acta 40, 296–306.

Olson, J.A., 2001. The motion of fibers in turbulent flow, stochastic simulation of isotropic homogeneous turbulence. Int. J. Multiphase Flow 27, 2083–2103.

Olson, J.A., Kerekes, R.J., 1988. The motion of fibers in turbulent flow. J. Fluid Mech. 377, 47–64.

Petrie, C.J.S., 1999. The rheology of fibre suspensions. J. Non-Newton. Fluid Mech., 87,369–87,402.

Petrich, M.P., Koch, D.L., Cohen, C., 2000. An experimental determination of the stress–microstructure relationship in semi-concentrated fiber suspensions. J. Non-Newton. Fluid Mech., 95,101–95,133.

Qi, D.W., 2001. Simulations of fluidization of cylindrical multi-particles in a three-dimensional space. Int. J. Multiphase Flow 27, 107–118.

Raiskinmaki, P., Shakib-Manesh, A., Koponen, A., Jasberg, A., Kataja, M., Timonen, J., 2000. Simulations of non-spherical particles suspended in a shear flow. Comput. Phys. Commun. 129, 185–195.

Rogers, M.M., Moser, R.D., 1992. The three-dimensional evolution of a plane mixing layer: the Kelvin–Helmoholtz roll-up. J. Fluid Mech. 243, 183–226.

Saffman, P.G., 1965. The lift on a small sphere in a slow shear flow. J. Fluid Mech. 22, 385–400.

Shams, M., Ahmadi, G., Rahimzadeh, H., 2001. Transport and deposition of flexible fibers in turbulent duct flows. J. Aerosol Sci. 32, 525–547.

Soltani, M., Ahmadi, G., 2000. Direct numerical simulation of curly fibers in turbulent channel flow. Aerosol Sci. Tech. 33, 392–418.

Soltani, M., Fan, F.-G., Ahmadi, G., Hart, S.C., 1997. Detachment of rigid-link fibers with linkage contact in a turbulent boundary later flow. J. Adhes. Sci. Technol. 11, 1017–1037.

Tong, X.-L., Wang, L.-P., 1999. Two-way coupled particle-laden mixing layer. Part 1: Linear instability. Int. J. Multiphase Flow 25, 575–598.

Turney, M.A., Cheung, M.K., McCarthy, M.J., Powell, R.L., 1995. Hindered settling of rod-like particles measured with magnetic resonance imaging. AIChE J. 41, 251–257.

Yamamoto, Y., Potthoff, M., Tanaka, T., Kajishima, T., Tsuji, Y., 2001. Large-eddy simulation of turbulent gas-particle flow in a vertical channel: effect of considering inter-particle collisions. J. Fluid. Mech. 442, 303–334.

Zettner, C.M., Yoda, M., 2001. Moderate-aspect-ratio elliptical cylinders in simple shear with inertia. J. Fluid Mech. 442, 241–266.

Zhang, H.-G., Ahmadi, G., Fan, F.-G., McLaughin, J.B., 2001. Ellipsoidal particles transport and deposition in turbulent channel flows. Int. J. Multiphase Flow 27, 971–1009.